PCCP

PAPER

View Article Online
View Journal | View Issue

Cite this: *Phys. Chem. Chem. Phys.*, 2025, **27**, 23802

Understanding the microwave heating properties of La–Ce–Ni oxides based on structural, dielectric, and conductive analysis

Tatsuya Hamashima,[a] Masateru Nishioka,[b] Takeharu Sugiyama,[c] Ken Watanabe,[d] Hajime Hojo[d] and Hisahiro Einaga *[d]

Received 14th June 2025,
Accepted 9th October 2025

DOI: 10.1039/d5cp02279g

rsc.li/pccp

Microwaves can selectively and rapidly heat materials upon absorption, offering advantages over conventional heating methods. However, practical applications in oxide materials remain limited due to insufficient understanding of fundamental heating mechanisms and inadequate control of heating characteristics. In this study, we elucidated the heating mechanism of La–Ce–Ni oxides to develop oxide materials with excellent microwave heating properties. We comprehensively investigated the crystal structure, microstructure, electrical conductivity, and dielectric properties of La–Ce–Ni oxides with various compositions. In La–Ce–Ni oxides, the strong CeO_2–$LaNiO_3$ interaction induced structural distortions and modified dielectric properties, which predominantly contributed the heating properties under a microwave electric field, rather than electrical conductivity. The dielectric properties, rather than the electrical conductivity, were the primary factors determining the microwave heating performance of this system.

Introduction

The industrial sector heavily relies on fossil fuels to generate large amounts of energy for heat.[1] Therefore, improving heat utilization efficiency is a crucial challenge for industrial decarbonization. Among various heating technologies, microwave heating is regarded as one of the most promising methods to achieve efficient heating.[2] This method offers several advantages, including (i) efficient internal heating, even in materials with low thermal conductivity; (ii) speed, thereby reducing the time to reach the target temperature; and (iii) selective heating, which minimizes unnecessary energy losses.[3–5] Indeed, the implementation of microwave heating in industrial processes has the potential to reduce energy consumption by approximately 60–80% compared to conventional heating.[2]

Many researchers have attempted to develop microwave-assisted catalytic processes.[6] For example, Krech *et al.* reported microwave-assisted oxidative methanol conversion in a heterogeneous sample at the pilot scale, demonstrating that power consumption could be reduced by nearly half compared to conventional methods during an 8 h operation.[3] In addition, microwave heating enhances catalytic performance, increasing the reaction rate by several times to as much as 1000-fold, improves selectivity, and suppresses byproduct formation.[4,5,7] Nevertheless, only a limited number of microwave-assisted processes have been successfully implemented in practical applications, with one of the main obstacles being the limitations of available catalytic materials. Conventional supports such as Al_2O_3, TiO_2, MgO, ZrO_2, and CeO_2 exhibit poor microwave heating properties,[8,9] resulting in underperformance in microwave-assisted catalytic systems. Carbon-based materials, as efficient microwave susceptors,[10,11] have been applied in various reactions, including organic synthesis and heterogeneous catalytic reactions such as NO_x and SO_2 reduction and methane decomposition. However, carbon-based materials react with the reactant under certain conditions, leading to limited durability.[10,12,13] The development of catalysts with excellent microwave heating properties, activity, and durability is required for highly efficient, microwave-assisted, solid–gas heterogeneous catalytic reactions.[14]

Notably, oxide catalysts, particularly those with good microwave heating properties, catalytic activity, and durability, have been employed in microwave-assisted catalytic processes. Among complex oxides containing transition metals, those incorporating Mn, Co, Cu, and Ni often exhibit relatively good microwave heating properties.[15] For instance, the $CuMnO_x$

[a] *Department of Interdisciplinary Engineering Sciences, Interdisciplinary Graduate School of Engineering Sciences, Kyushu University, Fukuoka 816-8580, Japan*
[b] *Minamo corporation, Miyagi 989-3127, Japan*
[c] *Kyushu University Synchrotron Light Research Center, Kyushu University, 6-1, Kasugakoen, Kasuga, Fukuoka 816-8580, Japan*
[d] *Department of Advanced Materials Science and Engineering, Faculty of Engineering Sciences, Kyushu University, Fukuoka 816-8580, Japan. E-mail: einaga.hisahiro.399@m.kyushu-u.ac.jp*

spinel oxide exhibited good performance in microwave-assisted benzene oxidation.[7]

Perovskite oxides, represented by the general formula ABO_3, can incorporate various elements into A and B sites, enabling fine-tuning of a wide range of physicochemical properties.[16] Thus, the microwave heating properties of perovskite oxides may be improved by controlling their dielectric properties, conductivity, and magnetic properties. Taking advantage of these characteristics, perovskite oxides with various constituents have been applied in microwave-assisted catalytic reactions, such as methane oxidation using La–Ce–Mn perovskite oxides,[17] bisphenol A degradation using $LaCuCoO_3$ catalysts,[18] CO oxidation using $LaMnO_3$, $LaCoO_3$, and $LaSrCoO_3$ catalysts,[19,20] and NO decomposition using $BaMnO_3$ and $BaCoO_3$ catalysts.[21,22]

Among perovskite oxides, $LaNiO_3$ is a promising catalyst owing to its high lattice oxygen reactivity and excellent CO oxidation activity under conventional heating conditions.[23] Furthermore, $La_{0.8}Ce_{0.2}NiO_3$ (where part of La in $LaNiO_3$ is substituted with Ce) exhibits excellent microwave heating properties, catalyzing CO oxidation with low energy consumption.[24] However, most previous studies have focused solely on correlating the composition with the bulk heating behavior, without clarifying the microscopic mechanisms that govern the dielectric and electrical conductivity. In particular, the role of interfacial interactions between coexisting phases has rarely been investigated previously. Therefore, although previous studies have suggested that the addition of Ce enhances the dielectric properties of oxide materials,[24] this does not sufficiently explain the heating mechanism, given that microwave heating properties are affected by multiple factors, including the crystal structure and electrical conductivity.[2,19] Hence, this study comprehensively investigates the effects of composition (*i.e.*, Ce/La ratio), electrical conductivity, and crystal structure on the microwave heating properties of La–Ce–Ni oxides to gain insights into the optimal design for microwave heating.

Experimental

Material preparation

La–Ce–Ni oxides were synthesized using a co-precipitation method, as described in the previous study.[24] The required amounts of $La(NO_3)_3{\cdot}6H_2O$ ($\geq$99.0%, Wako), $Ni(NO_3)_2{\cdot}6H_2O$ ($\geq$97.0%, Wako), and $Ce(NO_3)_3{\cdot}6H_2O$ ($\geq$98.0%, Wako) to synthesize $La_{1-x}Ce_xNiO_3$ (x = 0, 0.1, 0.2, 0.3, 0.4, 0.5, corresponding to Ce/La = 0, 1/9, 2/8, 3/7, 4/6, 5/5, respectively) were weighed and dissolved in deionized water. The resulting solution was then added dropwise to an aqueous tetramethylammonium hydroxide solution (10 wt%, Kishida) to obtain the hydroxide precipitates. The precipitates were stirred for 1 h and let settle for another 1 h. The resulting precipitate was filtered, dried, and subsequently calcined in an electric furnace at 850 °C for 5 h. As a reference sample of CeO_2, JRC-CEO-5 was obtained from the Catalysis Society of Japan.

Sample characterization

The crystal structures were measured using an X-ray diffractometer (Smart Lab, Rigaku Corporation, Japan) with Cu-Kα radiation, and the crystallite size was estimated using the Scherrer equation (K = 0.94) based on the XRD patterns. The specific surface areas of the samples were estimated using Brunauer–Emmett–Teller (BET) plots. The samples (0.1 g) were degassed in a vacuum at 200 °C for 1 h, followed by N_2 adsorption isotherms measured at −196 °C using BELSORP-mini (MicrotracBEL Corp., Japan). Scanning transmission electron microscopy (STEM) images were acquired using a JEM-ARM200F (JEOL Co., Ltd, Japan). X-Ray absorption fine structure (XAFS) measurements were performed at beamline BL06 of the Kyushu Synchrotron Light Research Center, Japan. The XAFS data were processed for background removal and normalization using Athena.[25]

Microwave heating

For the microwave heating experiments, a microwave generator (MR-2G-100, Ryowa Electronics Co., Ltd, Japan) was operated at 2.45 GHz with a maximum power of 100 W. Two distinct cavity configurations were utilized: (i) an electric field cavity, where the electric field intensity is maximized at the central axis of the resonator, and (ii) a magnetic field cavity, where the magnetic field intensity is maximized at the central axis. A quartz tube filled with the sample was placed at the center of the resonator. The detailed dimensions of the cavity, coupling mechanism, and sample positioning details are explained in (Fig. S1 and S2). After placing the sample, impedance matching was performed for each sample using a double slug tuner to minimize the reflected waves and ensure efficient power transfer. The microwave was irradiated at 20 W, obtained by subtracting the reflected microwave power from the irradiated microwave power. The coupling was retuned during microwave irradiation for each sample using a double slug tuner to minimize reflection and ensure efficient microwave transfer. To avoid shifts in the resonance frequency due to variations in the dielectric properties, the resonance frequency was automatically tuned during irradiation. The sample temperature was measured using an infrared pyrometer (TMHX-TME0050, Japan Sensor Corp., Japan) with an emissivity of 0.911. Each measurement was performed three times, and the results were averaged.

Measurements of relative dielectric constant of the samples

The relative dielectric constants of the samples were measured using the cavity perturbation method. Briefly, a quartz tube without sample was placed in the setup of the heating experiment, and the resonance frequency was measured. Subsequently, a quartz tube filled with sample was placed in the same setup and heated under dry air flow. The resonance frequency at the steady-state temperature was measured to obtain the dielectric constant. The cavity perturbation method offers several advantages: (i) it enables measurements to be taken using the same weight and shape of the sample as in microwave heating experiments, and (ii) it facilitates

measurements at high temperatures.[26] Thus, samples with same shape and weight as in the microwave heating experiments were placed in the same cavity under the same conditions. The acquired Q-factor and resonance frequency at each temperature were substituted into eqn (1) and (2) to obtain the dielectric constant (ε'_r) and dielectric loss factor (ε''_r), respectively, followed by calculation of the loss tangent ($\tan\delta$).[27]

Here, f_0 and f_L represent the resonance frequencies obtained before and after inserting the sample, respectively; V and ΔV refer to the internal volume of the cylindrical resonator and sample volume, respectively; and Q_0 and Q_L are defined as $Q_0 = f_0/\Delta f_0$ and $Q_L = f_L/\Delta f_L$, where Δf_0 and Δf_L are the half-widths of the resonance signals obtained before and after inserting the sample, respectively.

$$\varepsilon'_r = 1 + 0.539\frac{f_0 - f_L}{f_0}\frac{V}{\Delta V} \quad (1)$$

$$\varepsilon''_r = 0.539\left(\frac{1}{Q_L} - \frac{1}{Q_0}\right)\frac{V}{\Delta V} \quad (2)$$

The cavity perturbation method requires a small sample volume compared to the resonator volume, identical sample and resonator heights, the sample must have a thin rod shape, and the material must be homogeneous.[28] The packed samples could be assumed to be homogeneous given that they were randomly introduced. Filling the resonator to its full height with sample causes excessive perturbation of the electric field, leading to a substantial decrease in measurement accuracy,[28] whereas too little sample causes inaccurate temperature measurements, leading to inaccurate results. Therefore, measurements should be performed using an adequate quantity of sample. Herein, the same height of sample and glass tube was used for the heating experiments. Prior to measurement, the samples were heated at 600 °C for several minutes to remove moisture. The dielectric properties of the samples were measured in the range of 500 °C–600 °C.

Simulations of the electromagnetic field distribution and heat dissipation were conducted using COMSOL Multiphysics 6.1 software (COMSOL AB, Stockholm, Sweden). The electric field intensity and heat generation were simulated under microwave irradiation at 20 W based on the height of the packed sample in the quartz tube, dielectric constant, and dielectric loss factor, which were experimentally obtained.[29] Electrical conductivity measurements were performed using a VSP-300 potentiostat (BioLogic Science Instruments, Seyssinet-Pariset, France). The powdered samples were packed into a jig, and measurements were conducted at room temperature. The potential was swept from −0.05 to 0.05 V and −0.1 to 0.1 V, with a sweep rate of 200 mV s^{-1}, for $LaNiO_3$ and Ce-doped samples, respectively.

Results and discussion

Material characterization

Fig. 1 presents the X-ray diffraction (XRD) patterns of the samples prepared in this study. Distinct peaks corresponding to the perovskite phases were observed for the catalyst with Ce/La = 0. The intensities of peaks attributed $LaNiO_3$ decreased with increasing Ce/La ratio, whereas those attributed to CeO_2 and NiO increased, indicating that the added Ce did not form a perovskite structure but existed as CeO_2 within the samples. Peaks attributed to NiO were also detected in La–Ce–Ni oxides, and their intensities increased with increasing Ce/La ratio. These findings were consistent with those of previous studies reporting that the CeO_2 and NiO phases are segregated in La–Ce–Ni oxides.[30–32]

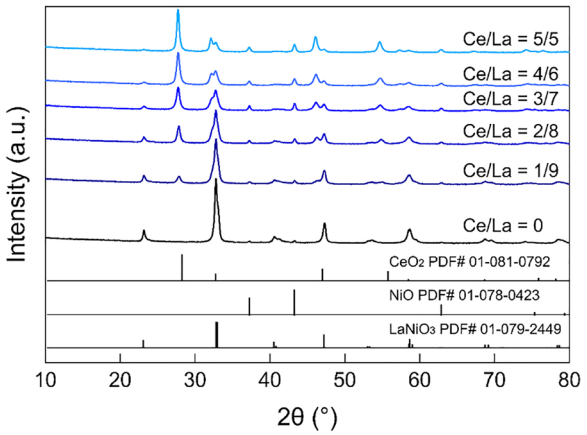

Fig. 1 XRD patterns of La–Ce–Ni oxides.

The crystallite size of $LaNiO_3$ tended to decrease with increasing Ce/La ratio (Table S1), likely due to the formation of an amorphous structure at the grain boundaries induced by Ce substitution or lattice mismatch with CeO_2. Additionally, the crystallite size of the CeO_2 phase increased with increasing Ce/La ratio, indicating the formation of well-defined CeO_2 crystallites.[33] For La–Ce–Ni oxides, the peak at approximately 59° attributed to $LaNiO_3$ slightly shifted toward a lower angle with increasing Ce/La ratio. Additionally, the peak split for the catalyst with Ce/La = 5/5, with a distinct additional peak observed (Fig. S3a). A similar trend was observed for the peak at approximately 33° (Fig. S3b). Furthermore, the peak at approximately 28° corresponding to CeO_2 shifted toward a lower angle with increasing Ce/La ratio (Fig. S3c). The prepared samples exhibited peak shifts toward a lower angle compared to the reference CeO_2 sample, which was attributed to the tensile strain caused by a stronger interaction between CeO_2 and $LaNiO_3$[33] facilitating oxygen vacancy formation due to weakened Ce–O bonds.[34] The observed shift in the peak corresponding to CeO_2 conflicted with previous studies reporting that the peak corresponding to CeO_2 shifted toward a higher angle in Ce-added $LaNiO_3$.[34] This discrepancy was likely due to differences in preparation processes, as citrate decomposition or the Pechini method was used in previous studies, which can induce different crystal structures.[35]

X-ray absorption fine-structure studies can provide information about the electronic states and local structures of materials. Fig. 2(a) presents the Ni K-edge X-ray adsorption near edge structure (XANES) spectra of La–Ce–Ni oxides. For all samples,

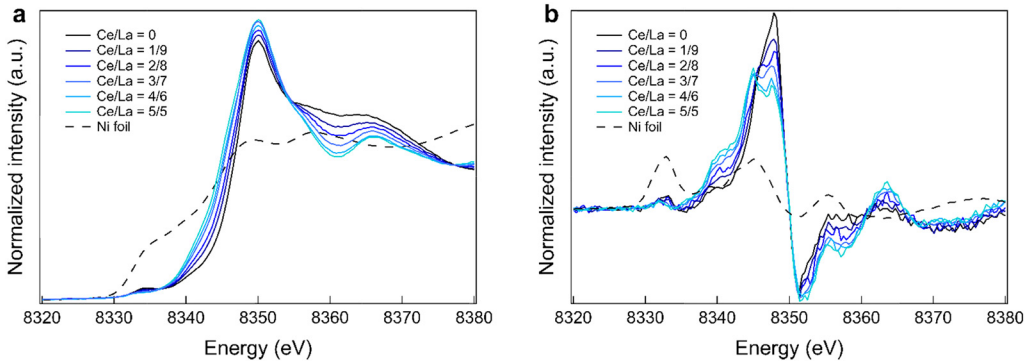

Fig. 2 Normalized Ni K-edge (a) XANES spectra and (b) first derivative XANES spectra of La–Ce–Ni oxides.

a pre-edge peak was observed at approximately 8.335 keV, corresponding to the quadrupole transition from Ni 1s to 3d.[36] The pre-edge peak height decreased with increasing Ce/La ratio owing to the increased density of 3d states.[36] Additionally, a shoulder peak was observed at approximately 8.340 keV in the first derivatives of XANES spectra (Fig. 2(b)). This shoulder peak, which is known to appear in reduced $LaNiO_3$, was attributed to transitions from 1s to 4pσ and 4pπ states. The energy splitting between 4pσ and 4pπ increased with decreasing Ni^{3+} concentration, causing the appearance of the shoulder peak in response to the changing valence state of Ni.[36] Hence, the absorption edge of each sample, defined as the energy at the midpoint of the edge step, was related to the Ni valence state (Table S2). The absorption edge shifted toward lower energy with increasing Ce/La ratio, suggesting a decrease in the Ni valence state.[37]

Fig. 3 presents the Fourier-transformed Ni K-edge extended XANES (EXAFS) spectra of the samples. The peak at approximately 1.5 Å corresponded to the Ni–O bond in $LaNiO_3$ and NiO, while that at approximately 3.1 Å corresponded to the Ni–O–La bond in $LaNiO_3$, and the shoulder peak observed at approximately 3.5 Å was attributed to the Ni–O–Ni bond within the perovskite structure.[23] The observation of these distinct peaks indicated that the sample was composed of perovskite structures. The peak at approximately 2.5 Å corresponded to the Ni–O–Ni bond in NiO, which was not detected for the catalyst with Ce/La = 0. By contrast, the intensity of the peak attributed to the Ni–O–Ni bond in NiO increased with increasing Ce/Ni ratio, whereas the intensity of the peak corresponding to the Ni–O–La bond in $LaNiO_3$ decreased. This finding indicated that the addition of Ce to $LaNiO_3$ caused the formation of an impurity phase, NiO, as observed in the XRD results. Scanning transmission electron microscopy (STEM) facilitated more detailed structural investigations of the La–Ce–Ni oxides. Fig. 4 presents the STEM images of the samples with Ce/La = 0 and Ce/La = 3/7. Ni segregated as NiO was observed in both samples and was more pronounced for the catalyst with Ce/La = 3/7. Furthermore, although less pronounced than that of NiO, partial segregation of CeO_2 was evident for the catalyst with Ce/La = 3/7. The STEM and XRD results were consistent. Bright-field images and electron diffraction patterns obtained from transmission electron microscopy (TEM) also clearly show the presence of $LaNiO_3$ and NiO phases in the sample with Ce/La = 0, and $LaNiO_3$, NiO, and CeO_{2-x} phases in the Ce-added sample

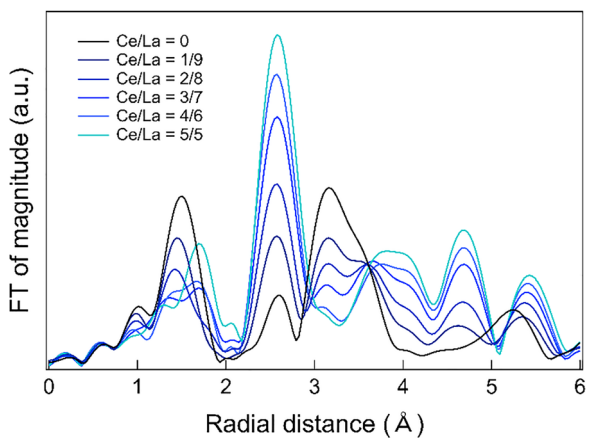

Fig. 3 Fourier transformed EXAFS spectra of La–Ce–Ni oxides.

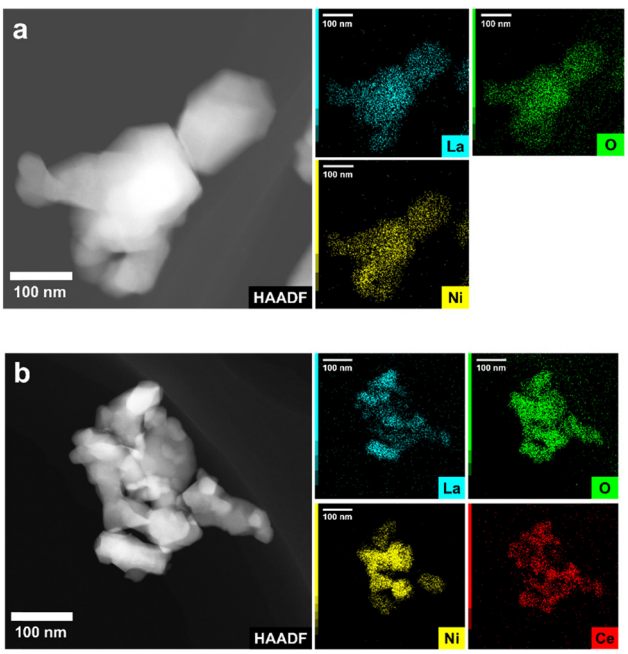

Fig. 4 STEM-EDS images of (a) Ce/La = 0 and (b) Ce/La = 3/7.

(Fig. S4 and S5). The specific surface area increased with Ce addition up to Ce/La = 2/8, as observed in previous research (Table S3).[24]

Heating properties of samples under electric field

To investigate the effect of the Ce/La ratio on the microwave heating properties of the La–Ce–Ni oxides, the samples were heated under a microwave electric field of 20 W obtained by subtracting the reflected microwave power from the irradiated microwave power (Fig. S6), and the acquired temperature profiles were averaged across three measurements (Fig. S7). The heating rate tended to increase with increasing Ce/La ratio (Table S4), and the samples reached an almost steady-state temperature after heating for 3 min. The steady-state temperature of the catalysts increased with increasing Ce/La ratio up to Ce/La = 3/7 and slightly decreased at higher Ce ratios (Fig. 5). In addition, we confirmed that the catalyst with Ce/La = 3/7 was reproducibly heated under microwave irradiation (Fig. S8). Although studies investigating microwave heating of graphite particles have shown that heat diffusion increases with increasing surface area,[38] no such correlation was observed with the prepared samples. The maximum temperature of a catalyst depends on the balance between heat transfer and microwave absorption, whereas the heating rate primarily depends on its microwave absorption properties.[38] Therefore, the catalyst with Ce/La = 3/7 exhibited efficient microwave absorption and optimal heat dissipation, resulting in the best microwave heating properties. Subsequently, we investigated the microwave heating properties of the catalysts with Ce/La = 0 and Ce/La = 3/7 under microwave powers of 15 and 25 W. The differences in the heating rate (Table S5) and steady-state temperature (Fig. S9) were more pronounced at higher microwave power.

To investigate the contribution of the impurity phases NiO and CeO_2 to the microwave heating properties of La–Ce–Ni oxides, $LaNi_{1.2}O_3$, $LaNi_{1.5}O_3$, $LaCe_{0.2}NiO_3$, and $LaCe_{0.5}NiO_3$ were prepared and subjected to microwave irradiation (Fig. S10). The steady-state temperature increased in the sample with excess Ni, but not significantly. By contrast, the sample with excess Ce exhibited a distinctly higher steady-state temperature, indicating that the contribution of segregated CeO_2 to microwave heating was more pronounced. Furthermore, the effect of physical contact between the $LaNiO_3$, NiO, and CeO_2 phases on heating performance was examined. CeO_2, NiO, and $LaNiO_3$ were calcined separately, followed by physical mixing using a mortar and pestle at an approximate Ni/La/Ce ratio = 1/0.7/0.3, and the physically mixed sample was heated under microwave irradiation, as previously described. The sample exhibited almost the same steady-state temperature as the catalyst with Ce/La = 0 (Fig. S12), suggesting that CeO_2 played a crucial role in enhancing the microwave heating properties of La–Ce–Ni oxides only when it was in close contact with $LaNiO_3$, potentially inducing distortion of the crystal structure, as discussed in the previous section.

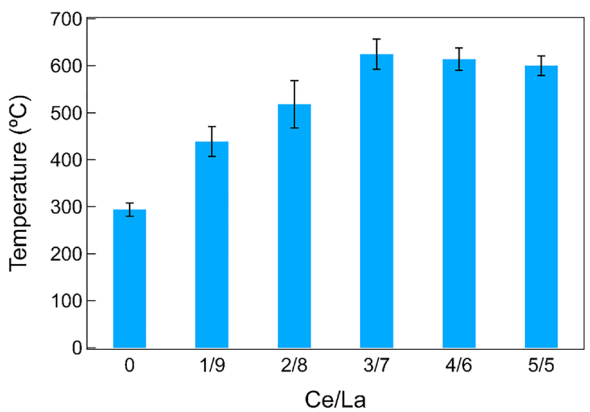

Fig. 5 Steady-state temperature after 3 minutes under microwave electric field heating at 20 W of microwave power.

Given that the crystallite size of $LaNiO_3$ decreased with increasing Ce/La ratio, potentially influencing the microwave heating properties of La–Ce–Ni oxides, we investigated samples with different crystallite sizes of $LaNiO_3$. $LaNiO_3$ was subjected to ball milling, as described by Uchiyama *et al.*,[39] and XRD analysis confirmed that the crystallite size of $LaNiO_3$ was reduced (Fig. S13). The sample was then sieved and microwave-heated. As shown in Fig. S14, the steady-state temperature of $LaNiO_3$ decreased after ball milling, suggesting that the reduction in crystallite size induced by Ce addition negatively affected the microwave heating properties of La–Ce–Ni oxides.

Dielectric properties of samples

The energy loss per unit volume of the material (denoted by P) is expressed by eqn (3).[2,40] Here, ω, μ_0, μ_r'', $|H|$, ε_0, ε_r'', σ, and $|E|$ refer to the electromagnetic wave frequency, vacuum permeability, imaginary part of complex permeability, magnetic field strength inside the material, vacuum permittivity, imaginary part of complex permittivity (ε_r^*), electrical conductivity, and electric field strength inside the material, respectively.

$$P = \frac{1}{2}\left(\omega\mu_0\mu_r''|H|^2 + \omega\varepsilon_0\varepsilon_r''|E|^2 + \sigma|E|^2\right) \quad (3)$$

In eqn (3), the first, second, and third terms represent magnetic, dielectric, and conductive losses, respectively.[2] Under an electric field, the second and third terms contribute to energy loss. Thus, the dielectric property (ε), magnetic property (μ), and electrical conductivity (σ) of the material are important parameters for explaining its microwave heating properties. However, given that separating the dielectric property and electrical conductivity is challenging, these terms are sometimes combined.[41,42] ε_r'' epresents the dielectric loss factor, which refers to the ability of a material to dissipate electromagnetic energy as heat, as expressed in eqn (4). By contrast, ε_r' is the real part of complex permittivity, which refers to the ability of a material to reversibly store electromagnetic energy.[41,43]

$$\varepsilon_r^* = \varepsilon_r' + j\varepsilon_r'' \quad (4)$$

The microwave absorption capability of the material can be determined using eqn (3) if the electric field can be measured inside the material (E). Otherwise, when the applied power is constant, the dielectric loss (the second term in eqn (3)) can be

expressed by eqn (5), using the electric field strength in air (denoted by E_a).[44]

$$P = \frac{1}{2}\omega\varepsilon_0 \tan\delta |E_a|^2 \quad (5)$$

The loss tangent ($\tan\delta$) is defined as the ratio of ε_r'' to ε_r', and similar to ε_r'', it represents the ability of a material to convert absorbed electromagnetic wave energy into heat.[41,45] Thus, these dielectric properties are crucial for evaluating the microwave heating properties of La–Ce–Ni oxides.

The accuracy of dielectric data is substantially influenced by factors such as the measurement method, sample quality, and dielectric property magnitude.[27] Miyakawa *et al.* reported that the obtained values were 30% higher when measuring the dielectric constant of ethylene glycol using this method compared to using a network analyzer, indicating an overestimation.[27] Consequently, the measured dielectric constants in this study were solely employed for comparison purposes among samples. As shown in Fig. 6(a), the value of the real part of the dielectric constant (ε_r') decreased with increasing Ce/La ratio, except for the catalyst with Ce/La = 3/7. By contrast, the value dielectric loss factor (ε_r'') exhibited an increasing trend with increasing Ce/La ratio, as shown in Fig. 6(b). However, the value of ε_r'' began to decrease when the Ce/La ratio exceeded 3/7. Notably, the contribution of the increase in ε_r'' surpassed that of ε_r' for $La_{0.7}Ce_{0.3}NiO_3$, resulting in the highest tanδ value (Fig. 6(c)).

To further understand the dielectric properties of La–Ce–Ni oxides, the temperature dependences of the dielectric constants ε_r' and ε_r'' were examined. According to the Debye equations, ε_r'' reaches its maximum when $\omega = 1/\tau$, where τ is the relaxation time, which is the time required for the ordered polarization induced by an external electric field to decay to $1/e$ of its initial value.[46] Given that τ depends on the polarization potential or other material properties, the peak frequency of ε_r'' varies with temperature and material composition. Thus, Ce addition may alter the polarization of the catalyst, resulting in different temperature dependences of ε_r'' and ε_r'. Furthermore, intermolecular bonds weaken with increasing temperature, leading to smaller τ values, and the ε_r'' peak consequently shifts toward higher frequencies.[44,47] However, no significant temperature dependence of ε_r'' was observed for any of the prepared catalysts, indicating that the influence of temperature was negligible within the measured range. Furthermore, the tanδ value exhibited a slight decreasing trend with increasing temperature, reflecting the slight temperature dependence of ε_r'.

Previous studies have suggested that ε_r'' is influenced by lattice defect sites, which affect the response of the material to an external electric field.[45] Zhang-Steenwikel reported that the formation of cation and oxygen vacancies could lead to an increase in ε_r' value in Ce-doped $LaMnO_3$ sample.[33] However, the La–Ce–Ni oxides in the present study exhibited the opposite trend, where an increase in the Ce/La ratio did not lead to an increase in ε_r'. To investigate the formation of oxygen lattice defects in La–Ce–Ni oxides, the dielectric properties of each sample were measured under different oxygen partial pressures.

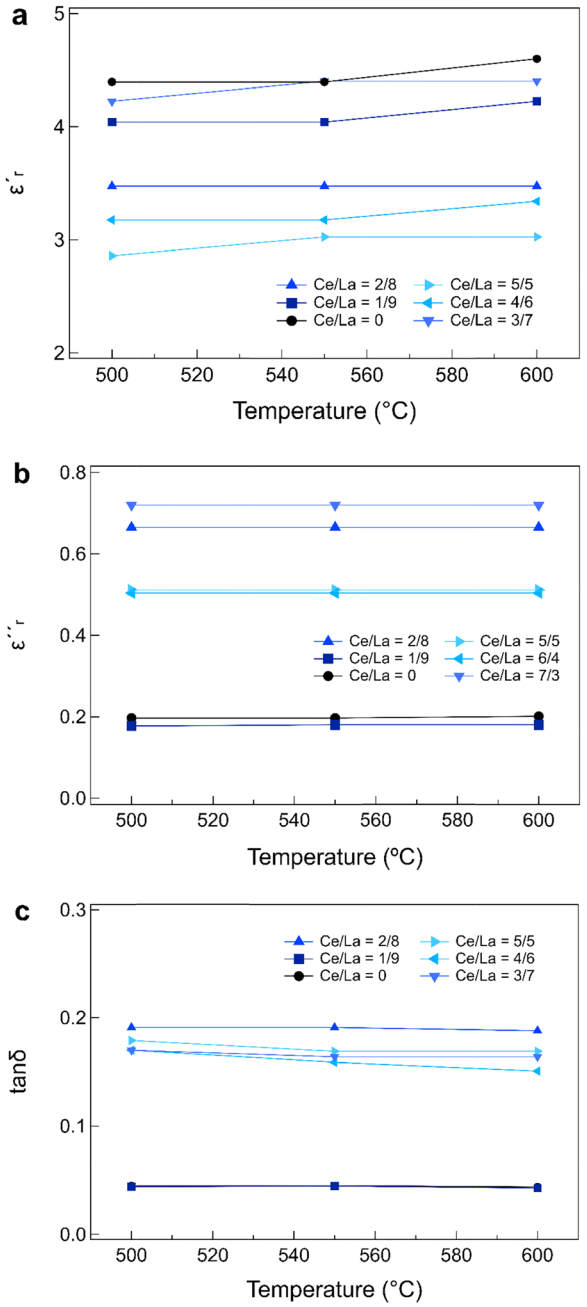

Fig. 6 Estimated (a) relative dielectric constant, (b) relative dielectric loss factor, and (c) loss tangent of La–Ce–Ni oxides using cavity perturbation method.

Specifically, the samples were heated under 100% N_2 or 100% O_2 gas flow, with the gas switched every 3 min, within the range of approximately 500 °C–550 °C, and their dielectric properties were measured every time the gas was switched (Fig. S15). Among the tested samples, the catalyst with Ce/La = 0 exhibited the most pronounced changes in dielectric properties and heating temperature. The steady-state temperature increased under the N_2 atmosphere, suggesting that the formation of oxygen vacancies enhanced the dielectric properties of the samples. By contrast, the catalyst with Ce/La = 3/7 maintained a relatively stable

temperature, regardless of the atmospheric conditions. The O_2-temperature programmed desorption experiment under microwave irradiation revealed an oxygen desorption peak at a lower temperature for the catalyst with Ce/La = 3/7 (Fig. S16), suggesting that oxygen defects were generated more easily. Close contact between the $LaNiO_3$ and CeO_2 phases in Ce-added samples caused lattice distortions with more stable lattice defects, resulting in a relatively weak response under varying oxygen partial pressures and good heating properties under microwave heating.

To examine the contribution of the dielectric properties to the heat dissipation of La–Ce–Ni oxides, the electric field distribution and heat generation within the samples were simulated using the obtained dielectric property values. Fig. 7 present the simulated electric field distributions for each sample, demonstrating that the electric field intensity inside the cavity tended to decrease with increasing Ce/La ratio. The average electric field strength within the microwave cavity (Fig. S18) decreased with increasing Ce/La ratio, and the catalyst with Ce/La = 3/7 exhibited the lowest value. The total power loss density within the samples, as shown in Fig. 8, also exhibited an increasing trend with increasing Ce/La ratio. Furthermore, the average power loss density reached its maximum value for the catalyst with Ce/La = 3/7 (Fig. S20). As shown by the electric field power density distribution within the samples, the power loss was significant at the lateral surfaces of all samples, suggesting that heat was concentrated around these regions.

In addition to the concentration of power loss at the lateral surfaces, depolarization effects are expected in the TM010 mode. These effects can weaken the net field inside the sample, particularly near the upper and lower planes, and decrease toward the center.[28] Although they were not experimentally analyzed in this study, they should be considered when interpreting the simulation results. In addition, this simulation assumed a uniform and insulating sample, whereas the actual samples were sieved samples, resulting in numerous vacant spaces. In addition, the samples exhibited electrical conductivity, as will be discussed in the following section. Therefore, the actual electric field and energy loss distribution may differ from the simulated results. Nevertheless, the heat generation values (Fig. S21) exhibited a similar trend as the microwave heating properties, indicating that dielectric loss led to efficient microwave absorption and heat generation.

Conductivity of samples

As previously discussed, dielectric loss generally includes conductive loss. However, separating these properties and determining whether heat generation is due to dielectric loss or conductive loss at a given frequency can be challenging.[44] Therefore, the dielectric loss factor may, in some cases, represent conductivity loss, as expressed in eqn (6).[42,48] Previous studies have reported that an increase in the dielectric loss factor can be attributed to its conductivity.[45,47–49]

$$\varepsilon = \varepsilon' - j\left(\frac{\sigma}{\omega} + \varepsilon''\right) \quad (6)$$

To examine the contribution of conductivity loss in the microwave frequency range, we performed microwave heating

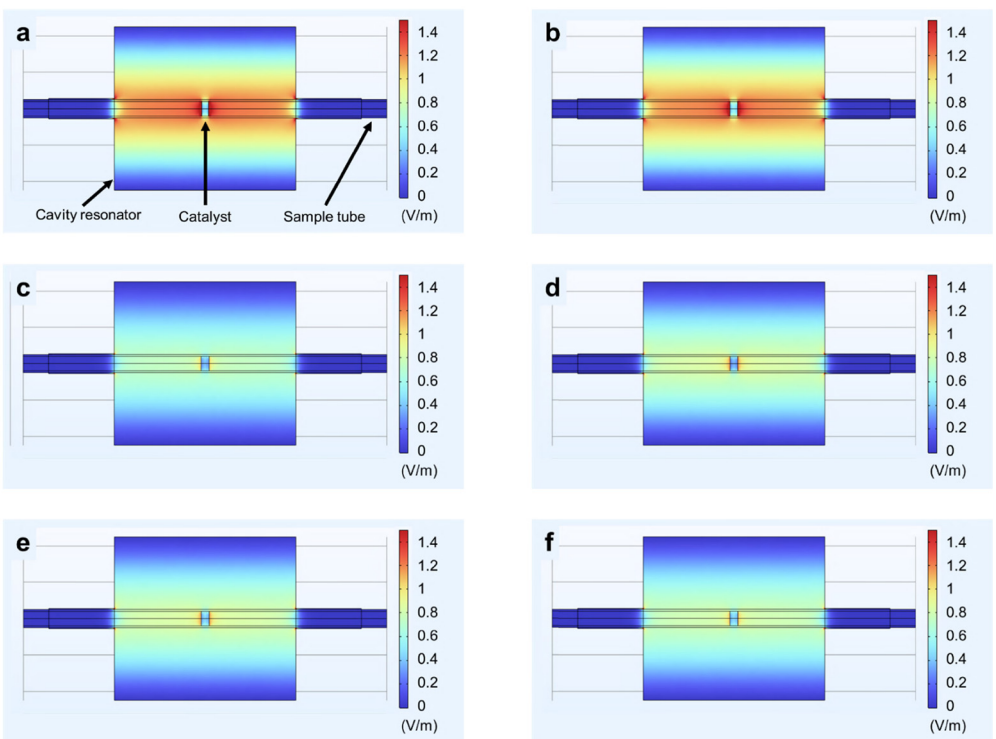

Fig. 7 Cross-sectional views of the simulated electric field strength within the reactor with Ce/La = (a) 0, (b) 1/9, (c) 2/8, (d) 3/7, (e) 4/6, and (f) 5/5.

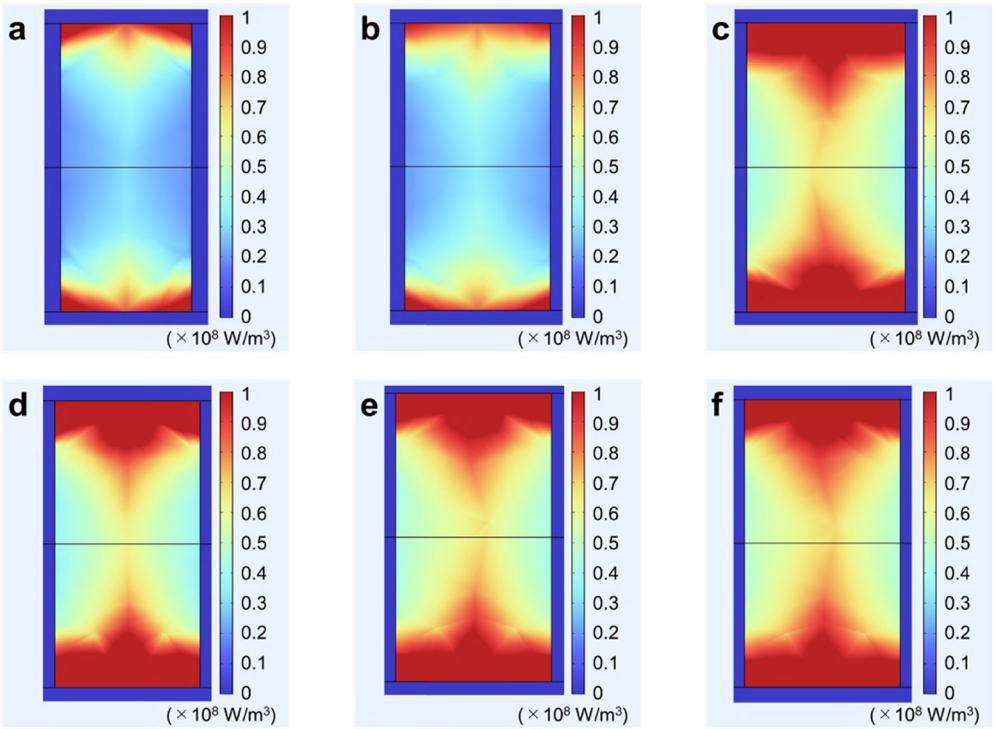

Fig. 8 Cross-sectional views of power loss density within the reactor with Ce/La = (a) 0, (b) 1/9, (c) 2/8, (d) 3/7, (e) 4/6, and (f) 5/5.

under a magnetic field at 20 W, obtained by subtracting the reflected microwave power from the irradiated microwave power (Fig. S22), and the temperature profiles of the samples were averaged over three measurements (Fig. S23). A rapid increase in temperature was observed with decreasing Ce/La ratio. The average heating rate of the samples when heated for 1–25 s (Table S6) clearly indicated that the addition of Ce did not promote the heating properties of the samples under a microwave magnetic field. In addition, the steady-state temperatures of the samples after 3 min of magnetic field heating at 20 W (Fig. 9) exhibited a decreasing trend with increasing Ce/La ratio, in contrast to that under the microwave electric field.

Materials that exhibit ferromagnetic or ferrimagnetic properties are heated through hysteresis loss at MHz frequencies and magnetic resonance heating at GHz frequencies,[50] whereas nonmagnetic materials such as aluminum and copper are known to be heated by eddy current loss.[51,52] Given that $LaNiO_3$ is a Pauli paramagnetic material known to exhibit relatively high electrical conductivity among metal oxide materials,[53–55] its heating mechanism under a magnetic field is likely due to eddy current loss. Therefore, the contribution of electrical conductivity loss to heating was evaluated based on the heating properties of La–Ce–Ni oxides under a magnetic field. The results were consistent with the direct current (DC) conductivity results, as shown in Fig. 9. The conductivity of the samples decreased with increasing Ce/La ratio, with $La_{0.7}Ce_{0.3}NiO_3$ exhibiting 0.02% of the conductivity of $LaNiO_3$. This significant decrease in conductivity can be attributed to the changes in the electronic structure induced by Ce substitution. $LaNiO_3$ exhibits relatively high conductivity due to the strong hybridization between the Ni 3d and O 2p orbitals, which form a metallic band structure.[56] Upon Ce addition, the average oxidation state of Ni decreased, thereby weakening the Ni 3d–O 2p orbital hybridization, as evidenced by the reduced pre-edge intensity in the Ni K-edge XANES. This disruption of the metallic band structure promotes electron localization, leading to the suppression of the electrical conductivity of La–Ce–Ni oxides.

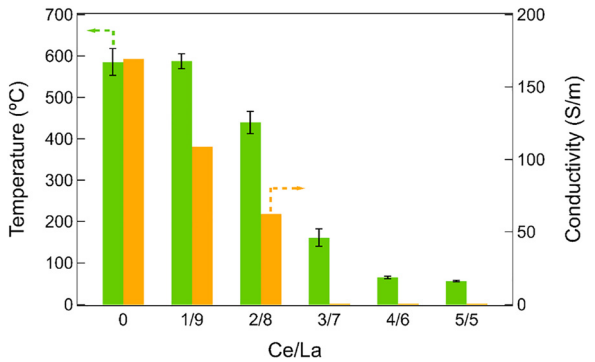

Fig. 9 Steady-state temperature after 3 min under microwave magnetic field heating at 20 W of microwave power and conductivity of sample.

The conductivity in the microwave frequency range should be represented as complex conductivity.[44,57] Indeed, AC electrical conductivity is affected by frequency, which is related to the space charge polarization.[58] When the microwave frequency is relatively low compared to the collision frequency of free electrons (*i.e.*, metals), it is possible to discuss sample

conductivity using DC conductivity without considering frequency dependences.[59] Thus, DC conductivity was utilized to estimate the microwave penetration depth of Cu and carbon.[48,52] Although the catalysts with Ce/La = 0 and Ce/La = 1/9 exhibited similar steady-state temperatures under the microwave magnetic field, the DC conductivity decreased. Several factors may explain the observed heating behaviors of these samples: (i) the presence of a weak electric field along the central axis of the TM 110 cavity, with magnetic loss potentially contributing to sample heating; and (ii) differing microwave penetration depths depending on the presence of an electric or magnetic field.[42]

In summary, CeO_2 segregated from the $LaNiO_3$ phase in La–Ce–Ni oxides and strongly interacted with $LaNiO_3$, causing distortion and reduced crystallite sizes of the CeO_2 and $LaNiO_3$ phases. This strong interaction was observed only in the co-precipitated samples and not in the physically mixed samples. The CeO_2–$LaNiO_3$ interaction contributed to the formation of stable lattice defect sites, resulting in dielectric property changes. However, no clear correlation was observed between crystallite size and the heating properties of La–Ce–Ni oxides under microwave electric field heating. Conversely, the incorporation of CeO_2 decreased the structural regularity, leading to poorer electrical conductivity and, consequently, reduced heating performance under microwave magnetic field heating. Although microwave heating consists of dielectric and conductive losses, the results of the study suggest that La–Ce–Ni oxides are primarily heated by dielectric loss.

Conclusions

The development of materials with excellent microwave heating properties is crucial for the practical application of microwave-assisted processes. This study investigated the mechanisms responsible for the excellent heating properties and catalytic activity of La–Ce–Ni oxides from a comprehensive perspective, including their dielectric properties, electrical conductivity, and crystal structure.

The prepared La–Ce–Ni oxides contained CeO_2 and NiO phases that coexisted with the $LaNiO_3$ phase, causing crystal distortion of the $LaNiO_3$ and CeO_2 phases. The heating properties of La–Ce–Ni oxides under an electric field increased with increasing Ce/La ratio, and the catalyst with Ce/La = 3/7 exhibited the highest steady-state temperature and heating rate. The superior heating performance of this oxide was not dependent on crystallite size but was strongly influenced by the CeO_2 phase, which was highly dispersed and in close contact with the $LaNiO_3$ phase, likely due to crystal distortion. The simulation results demonstrated the greatest energy loss and heat generation for Ce-added samples. By contrast, the electrical conductivity of La–Ce–Ni oxides significantly decreased with Ce addition, similar to the trend observed in steady-state temperatures under magnetic field heating, indicating that conductivity loss was less pronounced for Ce-added samples.

Future studies should investigate the lattice defects at the CeO_2–$LaNiO_3$ interface and the temperature distribution near the interface to obtain a more comprehensive understanding of the mechanism responsible for the observed excellent heating properties of La–Ce–Ni oxides. These insights will support the rational design of oxide materials for efficient microwave-assisted processes, including catalytic reactions, sintering of ceramics, and thermal processing of waste.

Conflicts of interest

The authors declare no competing financial interest.

Data availability

The data supporting the findings of this study, including microwave heating characteristics and dielectric properties of complex metal oxides, are available from the corresponding author upon reasonable request.

Supplementary information (SI): Catalyst preparation method, XRD, Heating properties, MS signals, Simulated data. See DOI: https://doi.org/10.1039/d5cp02279g.

Acknowledgements

This work was financially supported by JSPS KAKENHI grant number 21H03635.

References

1 M. Rehfeldt, T. Fleiter and F. Toro, A Bottom-up Estimation of the Heating and Cooling Demand in European Industry, *Energy Effic.*, 2018, **11**(5), 1057–1082.
2 A. Amini, M. Latifi and J. Chaouki, Electrification of Materials Processing via Microwave Irradiation: A Review of Mechanism and Applications, *Appl. Therm. Eng.*, 2021, **193**, 117003.
3 T. Krech, R. Krippendorf, B. Jäger, M. Präger, P. Scholz and B. Ondruschka, Microwave Radiation as a Tool for Process Intensification in Exhaust Gas Treatment, *Chem. Eng. Process.*, 2013, **71**, 31–36.
4 H. M. Nguyen, J. Sunarso, C. Li, G. H. Pham, C. Phan and S. Liu, Microwave-Assisted Catalytic Methane Reforming: A Review, *Appl. Catal., A*, 2020, **599**, 117620.
5 S. Horikoshi; K. Shimoda; K. Yoroizuka; M. Sato; N. Yoshikawa; A. Fujita; H. Hukushima; T. Mranaka; T. Chikata; A. Harada; K. Takeuch and R. Nagahata, *Microwave Science and Engineering*, S & T, Tokyo, 2018.
6 G. D. Stefanidis, A. N. Muñoz, G. S. J. Sturm and A. Stankiewicz, A Helicopter View of Microwave Application to Chemical Processes: Reactions, Separations, and Equipment Concepts, *Rev. Chem. Eng.*, 2014, **30**(3), 233–259.
7 S. Ding, C. Zhu, H. Hojo and H. Einaga, Enhanced Catalytic Performance of Spinel-Type Cu–Mn Oxides for Benzene Oxidation under Microwave Irradiation, *J. Hazard. Mater.*, 2022, **424**(Pt C), 127523.

8 J. M. Bermudez, B. Fidalgo, A. Arenillas and J. A. Menendez, Mixtures of Steel-Making Slag and Carbons as Catalyst for Microwave-Assisted Dry Reforming of CH_4, *Chin. J. Catal.*, 2012, **33**(7), 1115–1118.

9 B. Fidalgo, A. Arenillas and J. A. Menéndez, Mixtures of Carbon and Ni/Al_2O_3 as Catalysts for the Microwave-Assisted CO_2 Reforming of CH_4, *Fuel Process. Technol.*, 2011, **92**(8), 1531–1536.

10 T. T. Phuong Pham, K. S. Ro, L. Chen, D. Mahajan, T. J. Siang, U. P. M. Ashik, J. Hayashi, D. P. Minh and D. N. Vo, Microwave-assisted Dry Reforming of Methane for Syngas Production: A Review, *Environ. Chem. Lett.*, 2020, **18**, 1987–2019.

11 T. Kim, J. Lee and K.-H. Lee, Microwave Heating of Carbon-Based Solid Materials, *Carbon Lett.*, 2014, **15**(1), 15–24.

12 L. Li, X. Jiang, H. Wang, J. Wang, Z. Song, X. Zhao and C. Ma, Methane Dry and Mixed Reforming on the Mixture of Bio-Char and Nickel-Based Catalyst with Microwave Assistance, *J. Anal. Appl. Pyrolysis*, 2017, **125**, 318–327.

13 D. García and N. Stankiewicz, Syngas Production via Microwave-Assisted Dry Reforming of Methane, *Catal. Today*, 2021, **362**, 72–80.

14 V. Palma, D. Barba, M. Cortese, M. Martino and E. Meloni, Microwaves and Heterogeneous Catalysis: A Review on Selected Catalytic Processes, *Catalysts*, 2020, **10**(2), 246.

15 S. Horikoshi; R. F. Schiffmann; J. Fukushima and N. Serpone, *Microwave Chemical and Materials Processing: A Tutorial*, Springer, Singapore, 1st edn, 2017.

16 M. A. Peña and J. L. Fierro, Chemical Structures and Performance of Perovskite Oxides, *Chem. Rev.*, 2001, **101**(7), 1981–2017.

17 Y. Zhang-Steenwinkel, H. L. Castricum, J. Beckers, E. Eiser and A. Bliek, Dielectric Heating Effects on the Activity and SO_2 Resistance of $La_{0.8}Ce_{0.2}MnO_3$ Perovskite for Methane Oxidation, *J. Catal.*, 2004, **221**(2), 523–531.

18 W. Yin, W. Yun, Y. Lan, W. Ruotong and Z. Xiaodong, Highly Effective Microwave-Induced Catalytic Degradation of Bisphenol A in Aqueous Solution Using Double-Perovskite Intercalated Montmorillonite Nanocomposite, *Chem. Eng. J.*, 2020, **390**, 124550.

19 H. Einaga, Y. Nasu, M. Oda and H. Saito, Catalytic Performances of Perovskite Oxides for CO Oxidation under Microwave Irradiation, *Chem. Eng. J.*, 2016, **283**, 97–104.

20 D. Röhrens, A. Abouserie, B. Wang, G. Haselmann and U. Simon, Microwave-Assisted CO Oxidation over Perovskites as a Model Reaction for Exhaust Aftertreatment—A Critical Assessment of Opportunities and Challenges, *Catalysts*, 2022, **12**(7), 802.

21 W. Xu, N. Shi, Z. You, J. Cai, K. Peng, Z. Su and J. Zhou, Low-Temperature NO Decomposition through Microwave Catalysis on $BaMnO_3$-Based Catalysts under Excess Oxygen: Effect of A-Site Substitution by Ca, K and La, *Fuel Process. Technol.*, 2017, **167**, 205–214.

22 W. Xu, J. Cai, J. Zhou, Y. Ou, W. Long, Z. You and Y. Luo, Highly Effective Direct Decomposition of Nitric Oxide by Microwave Catalysis over $BaMeO_3$ (Me = Mn, Co, Fe) Mixed Oxides at Low Temperature under Excess Oxygen, *ChemCatChem*, 2016, **8**(2), 417–425.

23 H. Hojo, Y. Inohara, R. Ichitsubo and H. Einaga, Catalytic Properties of $LaNiO_3$ and Mn-Modified $LaNiO_3$ Catalysts for Oxidation of CO and Benzene, *Catal. Today*, 2022, **410**, 127–134.

24 T. Hamashima, T. Sugiyama, H. Hojo and H. Einaga, Microwave-Assisted CO Oxidation over $LaNiO_3$ and Ce-Promoted $LaNiO_3$, *J. Taiwan Inst. Chem. Eng.*, 2023, **158**, 105041.

25 B. Ravel and M. Newville, ATHENA, ARTEMIS, HEPHAESTUS: Data Analysis for X-Ray Absorption Spectroscopy Using IFEFFIT, *J. Synchrotron Radiat.*, 2005, **12**(Pt 4), 537–541.

26 K. Kashimura, H. Sugawara, M. Hayashi, T. Mitani and N. Shinohara, Microwave Heating Behavior and Microwave Absorption Properties of Barium Titanate at High Temperatures, *AIP Adv.*, 2016, **6**(6), 065001.

27 M. Miyakawa, S. Kanamori, K. Hagihara, A. Itagaki, T. Nakamura and M. Nishioka, Cylindrical Resonator-Type Microwave Heating Reactor with Real-Time Monitoring Function of Dielectric Property Applied to Drying Processes, *Ind. Eng. Chem. Res.*, 2021, **60**(25), 9119–9127.

28 C. Steiner, S. Walter, V. Malashchuk, G. Hagen, I. Kogut, H. Fritze and R. Moos, Determination of the Dielectric Properties of Storage Materials for Exhaust Gas Aftertreatment Using the Microwave Cavity Perturbation Method, *Sensors*, 2020, **20**(21), 6024.

29 Z. Ni, H. Hojo and H. Einaga, Comparative Evaluation of Microwave Heating Performance across Structurally Diverse Tungsten Oxides, *J. Phys. Chem. C*, 2024, **128**(33), 13807–13815.

30 A. Qi, S. Wang, G. Fu, C. Ni and D. Wu, La–Ce–Ni–O Monolithic Perovskite Catalysts Potential for Gasoline Autothermal Reforming System, *Appl. Catal., A*, 2005, **281**(1), 233–246.

31 S. M. Lima, J. M. Assaf, M. A. Peña and J. L. G. Fierro, Structural Features of $La_{1-x}Ce_xNiO_3$ Mixed Oxides and Performance for the Dry Reforming of Methane, *Appl. Catal., A*, 2006, **311**, 94–104.

32 S. Amini, F. Meshkani and M. Rezaei, Catalytic Oxidation of CO over Nanocrystalline $La_{1-x}Ce_xNiO_3$ Perovskite-Type Oxides, *Chem. Eng. Technol.*, 2019, **42**(11), 2443–2449.

33 Y. Zhang-Steenwinkel, H. L. Castricum, A. Bliek and E. Esveld, Perovskite-Type Oxides as Susceptor Materials in Dielectric Heating, *J. Mater. Sci.*, 2007, **42**(14), 5851–5859.

34 D. Ma, Z. Lu, Y. Tang, T. Li, Z. Tang and Z. Yang, Effect of Lattice Strain on the Oxygen Vacancy Formation and Hydrogen Adsorption at $CeO_2(111)$ Surface, *Phys. Lett. A*, 2014, **378**(34), 2570–2575.

35 Z. Gaoke, L. Ying, Y. Xia, W. Yanping, O. Shixi and L. Hangxing, Comparison of Synthesis Methods, Crystal Structure and Characterization of Strontium Cobaltite Powders, *Mater. Chem. Phys.*, 2006, **99**(1), 88–95.

36 J. C. Park, D. K. Kim, S. H. Byeon and D. Kim, XANES Study on Ruddlesden–Popper Phase, $La(N + 1)Ni(n)O(3n + 1)$ (N = 1, 2 and Infinity), *J. Synchrotron Radiat.*, 2001, **8**(Pt 2), 704–706.

37 R. J. Woolley, B. N. Illy, M. P. Ryan and S. J. Skinner, *In Situ* Determination of the Nickel Oxidation State in $La_2NiO_{4+\delta}$ and $La_4Ni_3O_{10-\delta}$ Using X-Ray Absorption near-Edge Structure, *J. Mater. Chem.*, 2011, **21**(46), 18592–18596.

38 K. Kashimura, N. Hasegawa, S. Suzuki, M. Hayashi, T. Mitani, N. Shinohara and K. Nagata, Effects of Relative Density on Microwave Heating of Various Carbon Powder Compacts Microwave-Metallic Multi-Particle Coupling Using Spatially Separated Magnetic Fields, *J. Appl. Phys.*, 2013, **113**(2), 024902.

39 T. Uchiyama, M. Nishibori, H. Einaga and Y. Teraoka, Formation of Tetravalent Fe Ions in $LaFeO_3$ Perovskite Through Mechanochemical Modification by Ball Milling, *J. Am. Ceram. Soc.*, 2015, **98**(4), 1047–1051.

40 K. Kawahira, Y. Saito, N. Yoshikawa, H. Todoroki and S. Taniguchi, Penetration Depth of Microwave into the Mixture of Goethite with Graphite Estimated by Permittivity and Conductivity, *Metall. Mater. Trans. B*, 2014, **45**(1), 212–220.

41 R. Rosa, P. Veronesi and C. Leonelli, A Review on Combustion Synthesis Intensification by Means of Microwave Energy, *Chem. Eng. Process.*, 2013, **71**, 2–18.

42 J. Sun, W. Wang and Q. Yue, Review on Microwave-Matter Interaction Fundamentals and Efficient Microwave-Associated Heating Strategies, *Materials*, 2016, **9**(4), 231.

43 P. Bhattacharya and C. K. Das, Investigation on Microwave Absorption Capacity of Nanocomposites Based on Metal Oxides and Graphene, *J. Mater. Sci.: Mater. Electron.*, 2013, **24**(6), 1927–1936.

44 S. J. Ichi; H. Sugiyama; C. Sato and M. Morizumi, *Electromagnetic Relations between Materials and Fields for Microwave Chemistry*, ed. H.-Z. Song, K. H. Yeap and M. W. C. Goh, IntechOpen, 2022.

45 A. Gupta and V. Choudhary, Electromagnetic Interference Shielding Behavior of Poly(Trimethylene Terephthalate)/Multi-Walled Carbon Nanotube Composites, *Compos. Sci. Technol.*, 2011, **71**(13), 1563–1568.

46 A. Zlotorzynski, The Application of Microwave Radiation to Analytical and Environmental Chemistry, *Crit. Rev. Anal. Chem.*, 1995, **25**(1), 43–76.

47 M. Hotta, M. Hayashi, M. T. Lanagan, D. K. Agrawal and K. Nagata, Complex Permittivity of Graphite, Carbon Black and Coal Powders in the Ranges of X-Band Frequencies (8.2 to 12.4 GHz) and between 1 and 10 GHz, *ISIJ Int.*, 2011, **51**(11), 1766–1772.

48 N. Yoshikawa, K. Kawahira, Y. Saito, H. Todoroki and S. Taniguchi, Estimation of Microwave Penetration Distance and Complex Permittivity of Graphite by Measurement of Permittivity and Direct Current Conductivity of Graphite Powder Mixtures, *J. Appl. Phys.*, 2015, **117**(8), 084105.

49 K. Kashimura, S. Suzuki, M. Hayashi, T. Mitani, N. Shinohara and K. Nagata, Surface-Plasmon-like Modes of Graphite Powder Compact in Microwave Heating, *J. Appl. Phys.*, 2012, **112**(3), 034905.

50 N. Yoshikawa and T. Kato, Ferromagnetic Resonance Heating of Fe and Fe_3O_4 by 5.8 GHz Microwave Irradiation, *J. Phys. D: Appl. Phys.*, 2010, **43**(42), 425403.

51 H. Fukushima, Microwave Processing and Applications to Future Automobile, *R&D Rev. Toyota CRDL*, 2015, **46**(3), 75–92.

52 M. Ignatenko, M. Tanaka and M. Sato, Absorption of Microwave Energy by a Spherical Nonmagnetic Metal Particle, *Jpn. J. Appl. Phys.*, 2009, **48**(6R), 067001.

53 Y. Tomioka, T. Ito, E. Maruyama, S. Kimura and I. Shindo, Magnetic and Electronic Properties of Single Crystals of Perovskite Nickelate Oxide $LaNiO_3$ Prepared by the Laser Diode Floating Zone Method, *J. Phys. Soc. Jpn.*, 2021, **90**(3), 034704.

54 J.-S. Zhou, L. G. Marshall and J. B. Goodenough, Mass Enhancement *versus* Stoner Enhancement in Strongly Correlated Metallic Perovskites: $LaNiO_3$ and $LaCuO_3$, *Phys. Rev. B: Condens. Matter Mater. Phys.*, 2014, **89**(24), 245138.

55 J.-S. Zhou, J. B. Goodenough and B. Dabrowski, Pressure-Induced Non-Fermi-Liquid Behavior of $PrNiO_3$, *Phys. Rev. Lett.*, 2005, **94**(22), 226602.

56 K. P. Rajeev, G. V. Shivashankar and A. K. Raychaudhuri, Low-Temperature Electronic Properties of a Normal Conducting Perovskite Oxide ($LaNiO_3$), *Solid State Commun.*, 1991, **79**(7), 591–595.

57 N. Yoshikawa; S. Junichi; M. Tomohiko; J. Fukushima; H. Takizawa; T. Shirai; K. Kashimura; H. Taira; M. Sato; N. Haneishi; Y. Wada; H. Kojima; M. Tsuji; M. Yoneya; H. Uchida; T. Fujitachi; S. Ouchi; S. Tsubaki; T. Yamada; H. Shimizu; Y. Nikawa; M. Asano; A. Higo; S. Mitsuru, Y. Toru, Y. Yasuji, Y. Mutsumi, T. Yasunori, W. Hisao, F. Hideoki, S. Horikoshi; K. Yamanaka; K. Iyomasa and N. Kuwahara, *Fundamentals and Industrial Application of Microwave Heating*, ed. S. Moriya, S&T Publishing Inc., Tokyo, 2017, vol. 1.

58 A. Algidsawi, A. Hashim, A. Hadi and M. Habeeb, Exploring the Characteristics of SnO_2 Nanoparticles Doped Organic Blend for Low Cost Nanoelectronics Applications, *Semicond. Phys., Quantum Electron. Optoelectron.*, 2021, **24**(04), 472–477.

59 N. Yoshikawa, *Introduction to Microwave Processing of Materials*, Corona Publishing Co., Ltd, Tokyo, 2014, vol. 1.